ARTICLES
https://doi.org/10.1038/s41563-021-01062-8

nature materials

Weyl-mediated helical magnetism in NdAlSi

Jonathan Gaudet[1,2,3] ✉, Hung-Yu Yang[4], Santu Baidya[5], Baozhu Lu[6], Guangyong Xu[2], Yang Zhao[2,3], Jose A. Rodriguez-Rivera[2,3], Christina M. Hoffmann[7], David E. Graf[8], Darius H. Torchinsky[6], Predrag Nikolić[1,9], David Vanderbilt[5], Fazel Tafti[4] and Collin L. Broholm[1,2]

Emergent relativistic quasiparticles in Weyl semimetals are the source of exotic electronic properties such as surface Fermi arcs, the anomalous Hall effect and negative magnetoresistance, all observed in real materials. Whereas these phenomena highlight the effect of Weyl fermions on the electronic transport properties, less is known about what collective phenomena they may support. Here, we report a Weyl semimetal, NdAlSi, that offers an example. Using neutron diffraction, we found a long-wavelength helical magnetic order in NdAlSi, the periodicity of which is linked to the nesting vector between two topologically non-trivial Fermi pockets, which we characterize using density functional theory and quantum oscillation measurements. We further show the chiral transverse component of the spin structure is promoted by bond-oriented Dzyaloshinskii–Moriya interactions associated with Weyl exchange processes. Our work provides a rare example of Weyl fermions driving collective magnetism.

Weyl semimetals are topologically non-trivial phases of matter that sustain low-energy excitations in the form of massless fermionic quasiparticles known as the Weyl fermions[1,2]. It is necessary to break either inversion[3–5] or time-reversal[6–11] symmetry to establish a Weyl semimetal. A rare occasion arises, however, if a material breaks both symmetries and offers an opportunity to study the interplay between magnetism and Weyl fermions[12–15]. Here we present an extensive experimental and theoretical study of a Weyl semimetal, NdAlSi, that breaks both symmetries. Our neutron diffraction experiment reveals that the leading instability of the Weyl semimetal is to long-wavelength incommensurate order, followed by a lower temperature transition to commensurate ferrimagnetism. Using quantum oscillation measurements and density functional theory (DFT), we find that the incommensurate wavevector connects different branches of the Fermi surface that contain Weyl fermions. This raises the interesting possibility of a magnetic order driven by relativistic electrons in NdAlSi.

Structural, magnetic and electronic bulk properties

Single crystals of NdAlSi were grown by a self-flux approach (Methods). The centred tetragonal unit cell and the first Brillouin zone of NdAlSi are shown in Fig. 1a,b. The structure breaks inversion symmetry, but site mixing between Al and Si can, however, restore a glide plane symmetry and change the space (point) group from non-centrosymmetic $I4_1md$ (C_{4v}) to centrosymmetric $I4_1/amd$ (C_{4h}). Contrary to X-ray scattering[16], the neutron scattering length (b) of Al and Si are sufficiently different (b(Al) = 3.449 fm, b(Si) = 4.1491 fm) that site mixing is readily apparent in neutron diffraction. The refinement of our single-crystal neutron diffraction pattern for NdAlSi in the $I4_1md$ space group is shown in Fig. 1c, while the atomic positions of each ion are reported in Supplementary Table 1. A better fit (with reduced chi-squared $\chi^2 = 5.70$) is obtained in $I4_1md$ compared to refinement in the $I4_1/amd$ space group ($\chi^2 = 6.04$), which yields a limit of 9% on Si–Al site mixing. The inset of Fig. 1c shows a strong second harmonic generation signal ($\chi_{xxz} = -115(3)$ pm V^{-1}, $\chi_{zxx} = 94(2)$ pm V^{-1} and $\chi_{zzz} = 564(5)$ pm V^{-1}) that originates from a bulk electric dipole and fits to the point group C_{4v}. Thus, we confirm that the non-centrosymmetric space group $I4_1md$ is correct for NdAlSi (Supplementary Fig. 1).

The magnetic heat capacity (C_p^{mag}) of NdAlSi is plotted in Fig. 1d, revealing a broad anomaly at approximately 18 K, as well as two peaks at a critical temperature of $T_{inc} = 7.2(1)$ K and $T_{com} = 3.3(1)$ K. A total entropy of $\Delta S = 0.96(2) \times R\ln(10)$ is released between 2.35 K and 300 K (inset of Fig. 1d), where R is the molar gas constant. This is the value expected for the ground-state spin–orbital manifold of Nd^{3+} with orbital angular momentum $L = 6$, spin $S = 3/2$ and total angular momentum $J = 9/2$. Fitting the temperature dependence of C_p^{mag} indicates splitting of the $2J + 1 = 10$-fold degenerate J multiplet into a ground-state doublet and four excited doublets at an energy gap $\Delta = 4(2)$ meV. The low-temperature anomalies at $T_{inc} = 7.2$ K and $T_{com} = 3.3$ K mark two magnetic phase transitions.

The temperature dependence of the inverse out-of-plane magnetic susceptibility ($1/\chi_c$) and its ratio with the in-plane susceptibility (χ_c/χ_a) are reported in Fig. 2a. An isotropic Curie–Weiss (CW) fit with a CW temperature $\Theta_{CW} = 10.2(8)$ K and an effective magnetic moment $\mu_{eff} = 3.65(5)\mu_B$, where μ_B is the Bohr magneton, describes the data well at high temperature, but fails at low temperature where the system develops an Ising-like easy axis anisotropy with $\chi_c/\chi_a > 80$ at $T = 1.8$ K. Comparing Fig. 1d and Fig. 2a shows that the signature of T_{inc} is clearer in the heat capacity, whereas T_{com} is most prominent in the magnetic susceptibility data. This is consistent with a putative antiferromagnetic (AFM) transition with a magnetic ordering vector $\mathbf{k} \neq 0$ at T_{inc} and a ferrimagnetic transition with $\mathbf{k} = 0$ at T_{com}. The magnetic transitions also affect the electrical resistivity (Fig. 2b), where the first small drop at T_{inc} and the second larger drop at T_{com}

[1]Department of Physics and Astronomy and Institute for Quantum Matter, The Johns Hopkins University, Baltimore, MD, USA. [2]NIST Center for Neutron Research, National Institute of Standards and Technology, Gaithersburg, MD, USA. [3]Department of Materials Science and Engineering, University of Maryland, College Park, MD, USA. [4]Department of Physics, Boston College, Chestnut Hill, MA, USA. [5]Department of Physics and Astronomy, Rutgers University, Piscataway, NJ, USA. [6]Department of Physics, Temple University, Philadelphia, PA, USA. [7]Neutron Scattering Division, Oak Ridge National Laboratory, Oak Ridge, TN, USA. [8]National High Magnetic Field Laboratory, Tallahassee, FL, USA. [9]Department of Physics and Astronomy, George Mason University, Fairfax, VA, USA. ✉e-mail: Jonathan.Gaudet@nist.gov

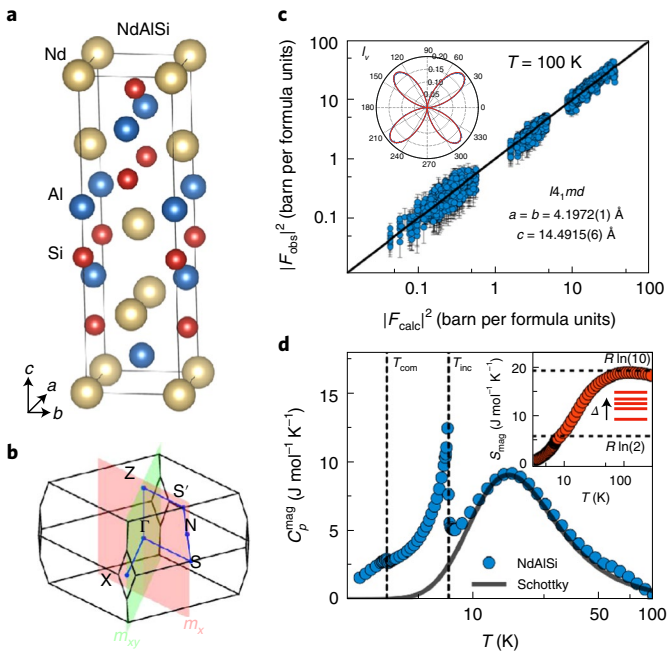

Fig. 1 | Crystal structure of NdAlSi. a,**b**, Structure of the non-centrosymmetric NdAlSi with space group $I4_1md$ (no. 109; **a**) and its associated first Brillouin zone shown in **b**. There are two simple mirror planes, m_x and m_y, and two glide mirrors, m_{xy} and $m_{x\bar{y}}$. These are shown in **b** as the light red and green planes, with the Z–Γ–X path lying in the green m_{xy} mirror plane and the Γ–S–N–S′–Z–Γ path lying in the red m_x mirror plane. **c**, Refinement of single-crystal nuclear neutron diffraction data collected at 100 K, where F_{obs} and F_{calc} are the observed and calculated structure factors, respectively. A black line of slope 1 is shown for visualization. Error bars are discussed in the Methods. The second harmonic generation signal (I_ν) is shown as an inset. **d**, Temperature dependence of the magnetic heat capacity (main panel) and magnetic entropy (S_{mag}) of NdAlSi (inset panel), which were isolated from the net heat capacity by subtracting the heat capacity of non-magnetic LaAlSi. The red lines represent an estimate of the energy scheme for the ground-state spin–orbit manifold of the Nd^{3+} ions in NdAlSi.

are correlated with the magnetic transitions. As explained below, the resistivity minimum at approximately 6 K correlates with the appearance of a third harmonic of the incommensurate order that is a precursor to the ferrimagnetic state observed for $T < T_{com}$. The resistivity changes observed across the magnetic phase transitions can occur due to differences in the spin excitations or to the Fermi surface or to the domain walls scattering.

Neutron diffraction and spin structure

The magnetic order parameters were determined through single-crystal neutron diffraction experiments that are summarized in Fig. 2c,d. Below T_{inc}, we found AFM Bragg peaks that are characterized by an incommensurate $\mathbf{k}_{inc} = (\frac{2}{3}+\delta, \frac{2}{3}+\delta, 0)$ ordering wavevector. We also observed magnetic Bragg peaks corresponding to the third harmonics of this wavevector, that is $\mathbf{k} = (3\delta, 3\delta, 0)$, whose intensity smoothly increases upon cooling from T_{inc} to T_{com}. The incommensurability $\delta(T)$ shows a weak temperature dependence before dropping to zero for $T < T_{com}$, where an abrupt transition to commensurate ferrimagnetic order occurs (Fig. 2d).

The spin polarization of both the ferromagnetic (FM) $\mathbf{k} = (0,0,0)$ and the AFM $\mathbf{k}_{com} = (\frac{2}{3}, \frac{2}{3}, 0)$ components of the $T < T_{com}$ ferrimagnetic spin structure were determined through refinement of magnetic neutron diffraction data (Supplementary Figs. 2 and 3). The primitive unit cell of NdAlSi contains two Nd ions located at positions $\mathbf{r}_1 = (0,0,0)$ and $\mathbf{r}_2 = (\frac{1}{2}, 0, \frac{1}{4})$ whose spin orientation and magnitude can differ in the ordered state. For the $\mathbf{k} = (0,0,0)$ component of the spin structure, however, such a difference would produce magnetic Bragg reflections at $\mathbf{k} = (1,1,0)$ positions, which are nuclearly forbidden in space group $I4_1md$ and are not present at any temperature in our data. Magnetic Bragg intensity was detected only at $\mathbf{k} = (0,0,0)$ positions such as the Bragg peak position $\mathbf{Q} = (1,0,1)$ (Fig. 3a). Furthermore, no magnetic Bragg intensity was detected at any of the $\mathbf{Q} = (0,0,l)$ Bragg peaks (such as $\mathbf{Q} = (0,0,4)$, shown in the inset of Fig. 3a). This precludes ordered in-plane components of the spins. Thus, we conclude that the $\mathbf{k} = (0,0,0)$ component of the commensurate low-T spin structure is ferromagnetic with spins oriented along the **c** direction (left inset of Fig. 3a).

The commensurate $\mathbf{k}_{com} = (\frac{2}{3}, \frac{2}{3}, 0)$ magnetism can be resolved in independent components polarized along the [110], [1$\bar{1}$0] and [001] real space directions. Each component of the magnetic moment on the $\mathbf{r}_1$ and $\mathbf{r}_2$ Nd sites of the chemical unit cell can either be parallel (+) or antiparallel (−) to each other. The latter two scenarios can be distinguished through neutron diffraction as + yields $\mathbf{Q}_+ = \mathbf{G} + (\pm 1/3, \pm 1/3, 0)$ Bragg peaks while − leads to $\mathbf{Q}_- = \mathbf{G} + (\pm 2/3, \pm 2/3, 0)$ peaks where $\mathbf{G}$ is any allowed nuclear Bragg peak. We found magnetic Bragg scattering at $\mathbf{Q}_-$ positions that is two orders of magnitude greater than at $\mathbf{Q}_+$, which indicates a dominant − state (Supplementary Fig. 3). The Ising anisotropy for this order was established by examining the $\hat{\mathbf{Q}}_- \cdot \hat{\mathbf{c}}$ dependence of the Bragg intensity (Fig. 3b) and shows this dominant component of the order is polarized along $\hat{\mathbf{c}}$, which is the unit vector of the lattice vector **c**. The $\hat{\mathbf{Q}}_+ \cdot \hat{\mathbf{c}}$ dependence of the Bragg intensity at $\mathbf{G} + (\pm 1/3, \pm 1/3, 0)$, on the other hand, shows this weak component of the spin structure is polarized along the $\hat{\mathbf{c}} \times \mathbf{k}$ direction and so along (1$\bar{1}$0) for $\mathbf{k} = (\pm 1/3, \pm 1/3, 0)$. This in-plane spin component is allowed by symmetry and is refined to a magnitude of $0.14(2)\mu_B$ per Nd (Supplementary Fig. 3). While we cannot determine the preferred handedness with unpolarized neutrons, this spin structure is chiral as indicated in Fig. 3c–e.

The $\mathbf{k} = (0,0,0)$ and $\mathbf{k}_{com} = (\frac{2}{3}, \frac{2}{3}, 0)$ components of the NdAlSi spin structure are respectively shown in the inset of Fig. 3a,b. Refined moment sizes of $1.1(2)\mu_B$ per Nd and $3.8(4)\mu_B$ per Nd were determined for the FM and AFM components, respectively. While the phase relationship between these components is unconstrained by diffraction, a constant moment requirement fixes the phase. The corresponding structure (Fig. 3c) can be described as a canted one-dimensional up–down–down (u–d–d) chain in Fig. 3d, where each arrow represents a plane of spins perpendicular to $\mathbf{k}_{com}$ (Fig. 3e).

The magnetization curve for the applied field $\mathbf{H} \| \mathbf{c}$ features two plateaus (Fig. 3f). The first plateau for applied field $\mu_0 H$ in the range $\mu_0 H_d = 0.1\,\mathrm{T} < \mu_0 H < \mu_0 H_c = 5.8\,\mathrm{T}$, with a net magnetization of $1.0(1)\mu_B$ per Nd is consistent with a single domain u–d–d state, where μ_0 is the electron magnetic moment. In agreement with the vanishing of $\mathbf{k}_{com}$ Bragg diffraction at H_c (Fig. 3f), the second plateau for $\mu_0 H > \mu_0 H_c = 5.8\,\mathrm{T}$ corresponds to the saturated state (u–u–u) with a magnetization of $2.9(1)\mu_B$ per Nd, which matches the sublattice magnetization of the zero-field u–d–d state as determined by diffraction.

Locally, the incommensurate spin structure of NdAlSi is also a canted Ising u–d–d structure (Supplementary Fig. 3), though with a long-wavelength amplitude modulation of 145(8) nm at $T = 3.5$ K. Incommensurate-to-commensurate phase transitions occur in many rare-earth and actinide intermetallics including UNi_2Si_2 (ref. [17]), CeNiAsO (ref. [18]) and CeSb (ref. [19]). Considering the exchange interactions and the strong easy axis anisotropy, mean field theory shows that amplitude-modulated incommensurate spin density wave ordering is generally unstable towards a lower T transition into a commensurate spin structure[20]. NdAlSi can be understood within this theoretical framework: An amplitude-modulated spin density wave with $\mathbf{k}_{inc} = (\frac{2}{3}+\delta, \frac{2}{3}+\delta, 0)$ first appears below T_{inc}, its amplitude

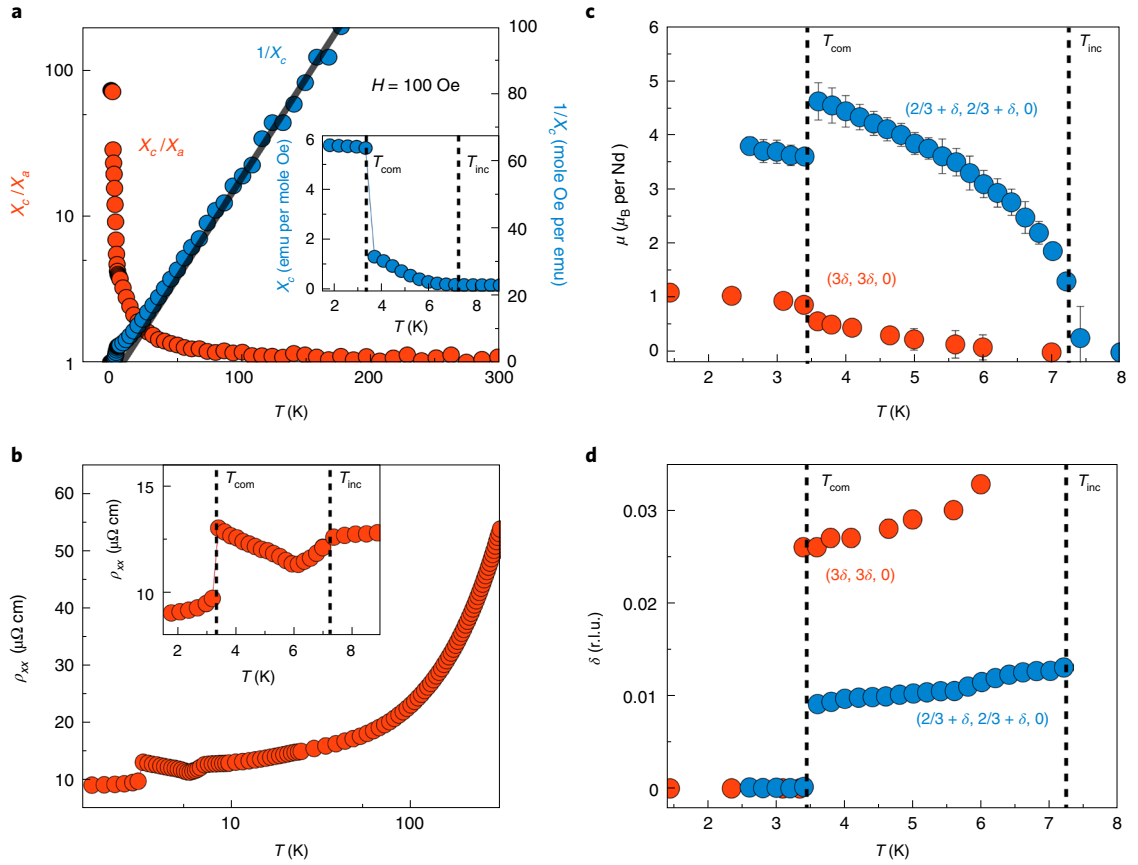

Fig. 2 | Magnetic phase transitions in NdAlSi. a, Temperature dependence of the inverse susceptibility for a field applied along the *c* axis (χ_c) as well as its ratio with the in-plane susceptibility (χ_a). The inset panels shows χ_c at low temperature. **b**, The *a*–*b* plane longitudinal electrical resistivity of NdAlSi versus temperature. A zoomed in picture of the electrical resistivity data at low temperature is in the inset. **c**,**d**, Respectively, the temperature dependence of the ordered moment and the associated wavevectors. For **c** and **d**, the blue data points were acquired at the $\mathbf{Q}=(2/3+\delta, 2/3+\delta, 0)$ incommensurate magnetic Bragg peak and were chosen to represent the order parameter for $(2/3+\delta, 2/3+\delta, 0)$, while the red data points are from $\mathbf{Q}=(1+3\delta, 1+3\delta, 2)$ and were chosen to represent the order parameter for $(3\delta, 3\delta, 0)$, where δ is the incommensurability in relative lattice units (r.l.u.). Error bars for **c** and **d** are discussed in the Methods.

growing upon cooling until T_{com}. As the amplitude grows, so does the third harmonic $\mathbf{k}=(3\delta, 3\delta, 0)$, which indicates that the sine wave is 'squaring up' and the magnitude of the moment on each site is becoming more constant through the lattice upon cooling. For an Ising-like incommensurate state, full magnetization on every site is expected at $T=0$, and it requires abrupt soliton-like defects. At T_{com} the commensurate u–d–d state with constant moment size per site becomes energetically favourable. Though its periodicity deviates slightly from that favoured by Fermi-surface nesting, the commensurate square-wave structure allows all Nd sites to achieve the saturation magnetization (Fig. 2c).

Quantum oscillations and band structure calculations

Magnetic interactions between rare-earth ions in metals are mediated by conduction electrons through the Ruderman–Kittel–Kasuya–Yosida (RKKY) mechanism. The often oscillatory character of the ordered state reflects the Fermi surface and the associated Lindhard susceptibility[21,22]. To make the connection between the modulated magnetism of NdAlSi and itinerant electrons, we combine DFT calculations and quantum oscillation experiments.

We present the field dependence of resistivity with $\mathbf{H} \parallel [001]$ in Fig. 3g. Shubnikov–de Haas (SdH) oscillations are observed at small fields. The pattern of SdH oscillations is visibly different in the AFM u–d–d phase for $H<H_c$ compared to the FM u–u–u phase for $H>H_c$. To extract the purely oscillatory part of the resistivity, $\Delta\rho_{xx}$, we subtract a smooth background from the $\rho_{xx}(H)$ curve at each temperature. The resulting $\Delta\rho_{xx}(H)$ curves are plotted as a function of $1/H$ in Fig. 4a (also Supplementary Fig. 6). Three phases with different oscillatory patterns are separated by dashed lines in Fig. 4a: the paramagnetic (PM) phase above T_{inc}, the FM u–d–d phase below T_{inc} and H_c and the FM phase below T_{inc} and above H_c. To extract the quantum oscillation frequencies, we performed a Fourier analysis in each phase, the result of which is shown in Fig. 4b–d. The peaks in Fig. 4d reveal oscillation frequencies in the PM phase with two characteristic frequencies, α and β. For $T<T_{com}$, however, only the α peak survives in the low-field u–d–d phase, while only the β peak survives in the FM phase (Fig. 4b,c).

We shall now establish a connection between the conduction electrons participating in quantum oscillations and the incommensurate atomic *f*-orbitals' magnetism by comparing the characteristic wavevector inferred from the SdH frequencies to the incommensurate ordering wavevector. The SdH frequencies are associated with the conduction electrons, and the ordering wavevector with the localized *f*-moment. The SdH oscillation frequencies F are related to the extremal orbit area (A_{ext}) on the Fermi surface via the Onsager relation $F=\frac{\phi_0}{2\pi^2}A_{ext}$, where ϕ_0 is the magnetic flux quantum. From here, we determine the characteristic reciprocal space dimension of the α and β orbits using $k_{\alpha,\beta}=\sqrt{A_{ext}}/\pi=\sqrt{2\pi F_{\alpha,\beta}/\phi_0}$ and plot these as a function of temperature along with the incommensurate component of the magnetic wavevector $q_\delta=\delta\sqrt{2}\mathbf{a}^*$ in

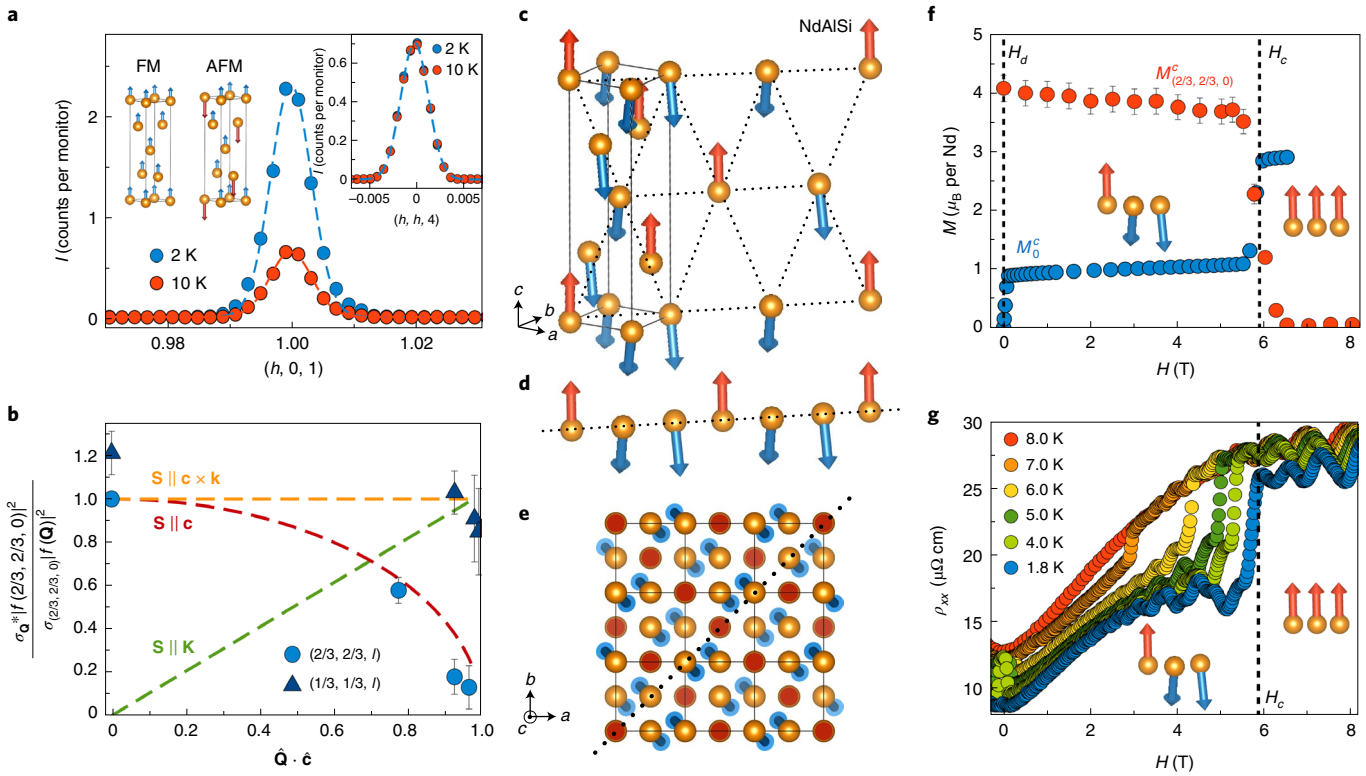

Fig. 3 | Commensurate ferrimagnetic spin structure of NdAlSi. a, Rocking scans at $\mathbf{Q}=(1,0,1)$ (main) and $\mathbf{Q}=(0,0,4)$ (right inset) whose magnetic intensities are consistent with the FM spin structure shown in the left inset. **b**, The $\hat{\mathbf{Q}}\cdot\hat{\mathbf{c}}$ dependence of the $\mathbf{Q}=(\frac{2}{3},\frac{2}{3},l)$ and $(\frac{1}{3},\frac{1}{3},l)$ Bragg peaks at $T=1.6$ K, which have been normalized to the $(\frac{2}{3},\frac{2}{3},0)$ Bragg peaks and multiplied by the ratio of their form factors $f(\mathbf{Q})$. The calculated $\hat{\mathbf{Q}}\cdot\hat{\mathbf{c}}$ dependence of the magnetic Bragg scattering intensity for three different spin polarizations is plotted and reveals the AFM $\mathbf{k}_{\rm com}=(\frac{2}{3},\frac{2}{3},0)$ component is polarized along $\hat{\mathbf{c}}$ whereas the $\mathbf{k}_{\rm com}=(\frac{1}{3},\frac{1}{3},0)$ component is polarized along $\hat{\mathbf{c}}\times\mathbf{k}$. Error bars are discussed in the Methods. **c**, A three-dimensional representation of the NdAlSi spin structure, which is obtained by adding the structures shown in the inset of **a**. The red (blue) arrows represent the Nd^{3+} up (down) spins. **d**, The effective one-dimensional spin configuration of **c** projected to $z=0$ and plotted along the [110] direction. **e**, The spin structure with the *c* axis coming out of the page. We note that for **c**–**e**, the spin canting has been amplified by a factor of six for visualization purposes. **f**,**g**, The *c* axis field dependence of the magnetization (M^c_0) as well as the AFM $\mathbf{k}_{\rm com}$ component at $T=1.6$ K ($M^c_{(2/3,\,2/3,\,0)}$) is shown in **f**, and the electrical resistivity is shown in **g** for various temperatures. The arrows in **f** indicate the transition from an AFM u–d–d to a FM u–u–u phase. Error bars represent ±1 standard deviation.

Fig. 4e, where $\mathbf{a}^*$ is the reciprocal lattice vector. All wavevectors vary smoothly with temperature, and the similarity of their rate of change with T (specifically $|\mathrm{d}k_{\alpha,\beta}/\mathrm{d}T|\approx|\mathrm{d}q_\delta/\mathrm{d}T|$) is consistent with a link between the incommensurate order and the Fermi surface of NdAlSi.

To explore this possibility, we performed DFT calculations (Methods) in the various magnetic phases of NdAlSi. For a robust determination of the Fermi energy $E_{\rm F}$ using quantum oscillation data, the DFT results are compared to SdH oscillations in the high-field FM state, the band structure of which is shown in Fig. 5a. For this calculation, the spin–orbit coupling is taken into account and the partially filled *f* orbitals are included in the valence. A large density of *f* states is obtained at the Fermi level without on-site interactions Hubbard U, but these are pushed away to lower and higher energies in the DFT + U calculations, where we have adopted $U=6$ eV (refs. [15,23]). In this case, a magnetic moment of $2.94\mu_{\rm B}$ per Nd is obtained, which is indistinguishable from the FM saturation magnetization (Fig. 3f) and the $2.9(1)\mu_{\rm B}$ per Nd sublattice magnetization of the commensurate low-T state determined by neutron diffraction.

We used the Wannier90 (ref. [24]) package to accurately interpolate the first-principles band structure (Methods). From here, we find a total of 56 Weyl nodes in this FM phase, whose locations within the first Brillouin zone are shown in Fig. 5b,c. The colours of the Weyl nodes reflect their chiralities, with red and blue dots representing nodes with chiralities +1 and −1, respectively. Because the magnetic point group has eight symmetry elements, the Weyl points come in groups of eight nodes that are all degenerate in energy, four with chirality +1 and four with chirality −1. We label the nodes as W_1 (one group), W_2 (two groups), W_3 (two groups), W'_3 (one group) and W''_3 (one group), accounting for a total of 56 Weyl nodes. The type and momentum space location of these Weyl nodes are strongly impacted by the *f*-electron magnetism. For example, Weyl nodes in the FM phase appear close to the glide mirror plane lying along the Γ–X direction. These arise due to the crossing of spin-up and spin-down bands, so they are not stabilized in the PM phase (Supplementary Figs. 4 and 5). Furthermore, Weyl nodes along the S′–Z direction change from type I to type II in going from the PM to the FM phase.

Having presented the quantum oscillations and DFT calculations for NdAlSi, we now combine these to obtain the Fermi surface in the FM state (Fig. 5d,e). The Fermi level was determined by comparing the calculated β frequency from DFT and the experimental value of k_β from quantum oscillations, as well as two other quantum oscillation frequencies that were resolved in our high-field experiment (γ and Σ in Supplementary Fig. 6). The best agreement was obtained with $E_{\rm F}-E_{\rm F}^{\rm DFT}=+30(3)$ meV, where $E_{\rm F}^{\rm DFT}=6.7473$ eV is the charge-neutrality point. The parts of the resulting Fermi surface that support the extremal orbit β, γ and Σ are indicated in Fig. 5d,e.

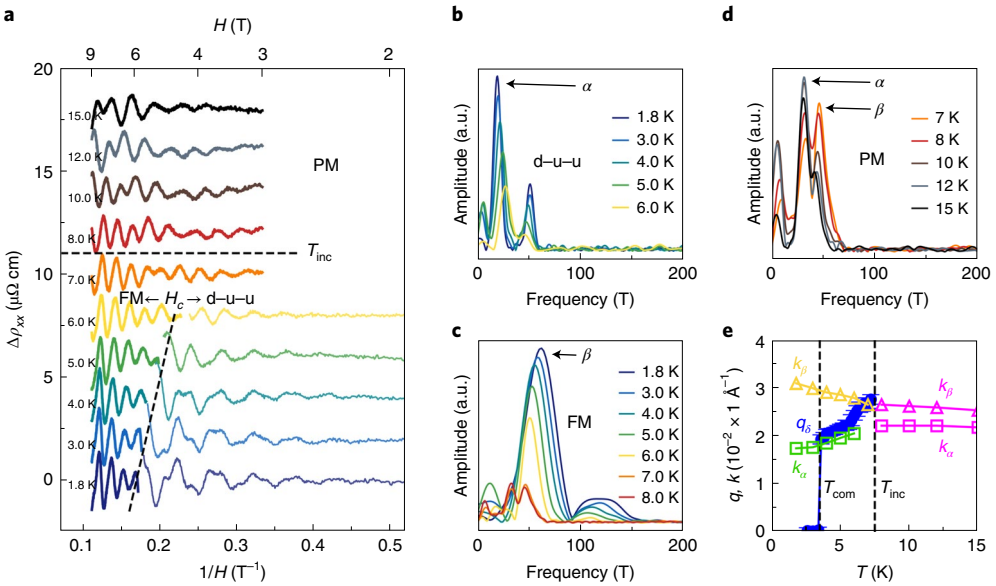

Fig. 4 | Quantum oscillations in NdAlSi. a, Quantum oscillations recorded above and below the transition temperature $T_{inc}(H=0)$, separated by the horizontal dashed line, and above and below the metamagnetic transition field H_c, separated by the slanted dashed line. **b**–**d**, The fast Fourier transform (FFT) spectra of the oscillations for the AFM $(\frac{2}{3}, \frac{2}{3}, 0)$ phase, the FM phase and the PM phase are respectively shown in **b**, **c** and **d**. **e**, The temperature evolution of the magnetic incommensurability q_δ (Fig. 2), and quantum oscillation frequencies k_α and k_β in different phases. Note that the SdH frequencies are displayed as $k = \sqrt{A_{ext}/\pi}$ where A_{ext} is the inferred area of the extremal orbit.

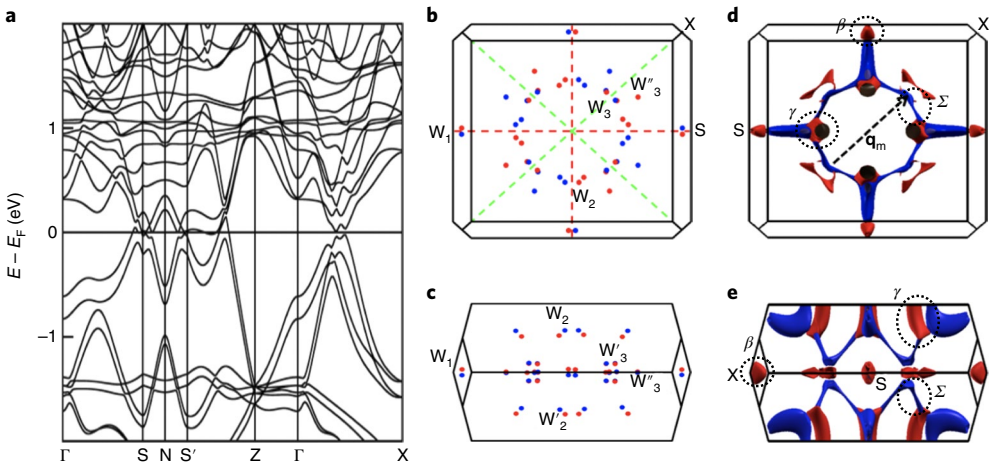

Fig. 5 | DFT + *U* electronic structure for the ferromagnetic phase of NdAlSi including spin–orbit coupling. a, Band structure. **b**,**c**, Weyl nodes in top and side view, respectively, along **a***. The six types of Weyl nodes are marked as W_1, W_2, W'_2, W_3, W'_3 and W''_3. Red and blue Weyl points have opposite chirality. **d**,**e**, Respectively, the top and side view of the Fermi surface with the Fermi energy set to be consistent with the quantum oscillation frequencies as described in the text. The red (blue) surfaces represent the valence (conduction) band. The dotted circles in **d** and **e** show the Σ, β and γ Fermi pockets characterized by quantum oscillations (Fig. 4).

Incommensurate magnetism and nesting wavevector

The $\mathbf{k}_{inc} = (\frac{2}{3}+\delta, \frac{2}{3}+\delta, 0)$ magnetic order of NdAlSi is unique among the reported RAlSi/RAlGe compounds (where R is a rare-earth ion), where so far only commensurate $\mathbf{k}=0$ orders were reported in the zero field[13–15]. To understand the origin of this modulated magnetic order, we note that the Fermi surface for FM NdAlSi includes pockets near $\mathbf{Q} = (\pm\frac{1}{3}, \pm\frac{1}{3}, l)$ with both $l=0$ and $l\neq0$ (Fig. 5d,e). Nesting between symmetrically equivalent diagonal pairs of these pockets might be responsible for the instability of the FM state towards formation of the $\mathbf{k}_{inc} = (\frac{2}{3}+\delta, \frac{2}{3}+\delta, 0)$ spin density wave for $H<H_c$ (the nesting vector, $\mathbf{q}_m$ in Fig. 5d).

A quantitative comparison of the nesting vector $\mathbf{q}_m$ and the magnetic ordering vector is presented in Fig. 6a. For this figure, we generated the Fermi surface of FM NdAlSi for a wide range of E_F and extracted the extremal positions of the l-integrated Fermi pockets lying along (110). The minimum and maximum extremal positions of these pockets were then multiplied by two to define the range of possible nesting vectors (Fig. 6b) bounded by the green region between $q_{min}(E_F)$ and $q_{max}(E_F)$ in Fig. 6a. The vertical blue bar in Fig. 6a represents the value of E_F that was independently determined by the quantum oscillation analysis, while the horizontal red bar is k_{inc} from neutron diffraction. The red and blue lines meet in the

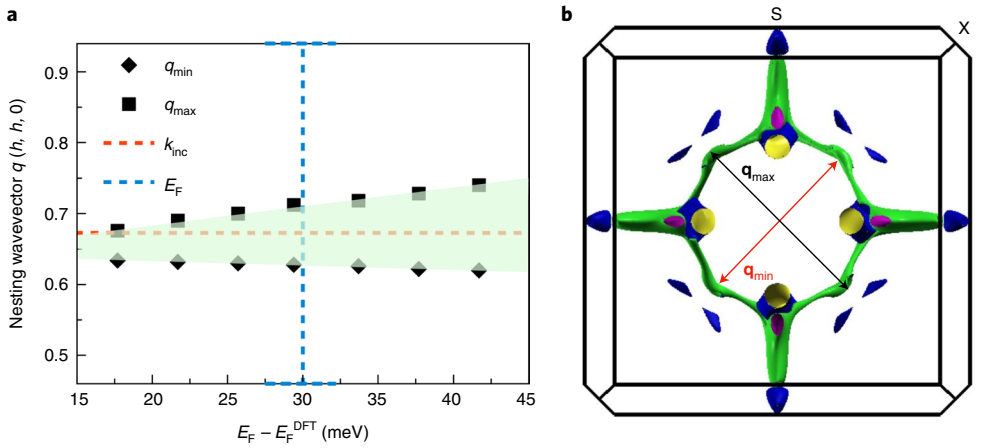

Fig. 6 | Nesting vector and the $(\frac{2}{3}+\delta, \frac{2}{3}+\delta, 0)$ magnetic order in NdAlSi. a, The black dots represent the minimum (q_{min}) and maximum (q_{max}) momentum vectors connecting two Fermi pockets of NdAlSi that lie along the (hh0) or Γ–X direction of the first Brillouin zone. The green region encompasses all possible nesting vectors versus $E_F - E_F^{DFT}$, where E_F^{DFT} is the charge-neutrality level. The red line indicates the $(\frac{2}{3}+\delta, \frac{2}{3}+\delta, 0)$ magnetic wavevector detected by neutron diffraction in NdAlSi and the blue line is the value of $E_F - E_F^{DFT}$ obtained from our quantum oscillation analysis. The horizontal blue bars represent the error bars on $E_F - E_F^{DFT}$, for which we provide further details in the Supplementary Information (Supplementary Fig. 6). **b**, Fermi surface of FM NdAlSi for $E_F - E_F^{DFT} = 33$ meV with arrows indicating $\mathbf{q}_{min}$ and $\mathbf{q}_{max}$ used for the analysis presented in **a**.

green region, where nesting conditions are satisfied. This indicates that the nesting between Fermi pockets lying along (110) could be responsible for the magnetic order observed in NdAlSi. We note that this result is not the fruit of a fine tuning of E_F since the nesting condition is satisfied over a broad range of E_F, which extends well beyond the constraints of our quantum oscillation analysis.

We can then rationalize the low-temperature magnetic order starting from the FM state where the Zeeman term completely dominates and all the spins point along the $\boldsymbol{c}$ axis. Upon decreasing the field to H_c, the magnetic susceptibility develops a peak at $\mathbf{k}_{inc}$ due to RKKY interactions that favour the nesting wavevector. At still lower fields, the corresponding modulated and weakly canted magnetic order emerges to gap the soft mode. This phenomenology is well established for various rare-earth metallic and intermetallic systems[21,22].

Discussion and conclusion

NdAlSi is special in that the nesting Fermi pockets contain W_3 Weyl nodes that are 41 meV above E_F (Fig. 5b,c). Weyl-mediated RKKY interactions have been studied using perturbation theory[25–30]. Every pair of Weyl nodes separated by a wavevector $\mathbf{q}$ contributes Heisenberg, Kitaev and Dzyaloshinskii–Moriya interactions among local moments. The Heisenberg coupling $J(\delta\mathbf{r})$ between two moments a distance $\delta\mathbf{r}$ apart features sign-changing spatial modulations with wavevector $\mathbf{q}$ and a rapid attenuation at larger distances $|\delta\mathbf{r}| > \hbar/\Lambda$, where Λ is the momentum cut-off in the relativistic dispersion of Weyl electrons and ħ is the Planck constant. The overall $J(\delta\mathbf{r} \to 0) < 0$ from equal-chirality Weyl nodes promotes a spin density wave at $\mathbf{q}$ while every single node yields a $\mathbf{q} = 0$ ferromagnetic channel through intra-node electron scattering. This latter interaction naturally explains the $\mathbf{k}_{FM} = 0$ spin component that ultimately develops in NdAlSi, as it is favoured by every Weyl hole and electron pocket.

The AFM spin component can arise from inter-node scattering processes. The multitude of Weyl nodes in NdAlSi creates many potential AFM ordering channels from which only the $\mathbf{k}_{inc} = \left(\frac{2}{3}+\delta, \frac{2}{3}+\delta, 0\right)$ order actually arises. To understand its selection, we note that nearly commensurate nesting wavevectors produce orders that support saturated sublattice magnetization and therefore are energetically favoured. Moreover, $\mathbf{k}_{inc}$ approximately connects not one but four symmetry-related pairs of W_3 Weyl nodes. Furthermore, the third harmonic $3\mathbf{k}_{inc}$, which must be present in a sublattice-saturating square-wave state and was observed at $(3\delta, 3\delta, 0)$ (Fig. 2c), is near the Γ point. Thus, in contrast to other Weyl–Weyl ordering channels, the third harmonic of $\mathbf{k}_{inc}$ is favoured by $\mathbf{q} \to 0$ intra-node scattering.

The observation of a chiral spin texture in NdAlSi points to sizeable Dzyaloshinskii–Moriya interactions, which are predicted by the Weyl-mediated RKKY coupling. The Dzyaloshinskii–Moriya vector associated with a pair of spins is furthermore predicted to lie parallel to their displacement[26,28,30]. The low-T spin structure we observe in NdAlSi can be stabilized by an easy axis crystal field term, sizeable AFM first and second nearest-neighbour exchange interactions and weaker first and second nearest-neighbour Dzyaloshinskii–Moriya interactions constrained by the Weyl–RKKY coupling to lie along the bond vectors. Weyl-mediated RKKY interactions thus provide a coherent provisional explanation of the observed magnetic order in NdAlSi (also Supplementary Fig. 7).

In conclusion, we have discovered an incommensurate magnetic ordering in NdAlSi, an inversion-symmetry-breaking semimetal with topologically protected Weyl nodes. Upon cooling, the magnetic wavevector $\mathbf{k}_{inc} = (\frac{2}{3}+\delta, \frac{2}{3}+\delta, 0)$ approaches the commensurate point $(\delta \to 0)$ while the third harmonic grows and the incommensurate structure acquires square-wave character. This culminates in a phase transition to low-T commensurate chiral ferrimagnetism with characteristic wavevectors $\mathbf{k} = (0, 0, 0)$, $(\frac{1}{3}, \frac{1}{3}, 0)$ and $(\frac{2}{3}, \frac{2}{3}, 0)$. Low-field temperature-dependent quantum oscillations of the magnetoresistance links $\delta(T)$ to the characteristic linear dimension of the Fermi surface. Through DFT + U calculations we establish the Fermi surface of the field-driven ferromagnetic state, determining the chemical potential through comparison of extremal orbital areas to SdH oscillation frequencies. The $\mathbf{k}_{inc}$ is found to approximately connect four pairs of Weyl nodes and the small associated Fermi pockets. While Ising like with moments predominantly along $\hat{\mathbf{c}}$, the low-T ferrimagnetic structure has a small transverse component that renders the ordered state chiral. These observations indicate the magnetic order in NdAlSi is driven by Weyl exchange interactions: inter- and intra-Weyl point processes favouring $\mathbf{k}_{inc}$ and $\mathbf{k} = (0, 0, 0)$, respectively. Our work provides a concrete example of collective magnetism driven by Weyl fermions.

Online content

Any methods, additional references, Nature Research reporting summaries, source data, extended data, supplementary information, acknowledgements, peer review information; details of author contributions and competing interests; and statements of data and code availability are available at https://doi.org/10.1038/s41563-021-01062-8.

Received: 23 December 2020; Accepted: 23 June 2021;
Published online: 19 August 2021

References

1. Armitage, N. P., Mele, E. J. & Ashvin, V. Weyl and Dirac semimetals in three-dimensional solids. *Rev. Mod. Phys.* **90**, 015001 (2018).
2. Wan, X., Turner, M. A., Vishwanath, A. & Savrasov, S. Y. Topological semimetal and Fermi-arc surface states in the electronic structure of pyrochlore iridates. *Phys. Rev. B* **83**, 205101 (2015).
3. Lv, B. Q. et al. Experimental discovery of Weyl semimetal TaAs. *Phys. Rev. X* **5**, 031013 (2015).
4. Yang, L. X. et al. Weyl semimetal phase in the non-centrosymmetric compound TaAs. *Nat. Phys.* **11**, 728–732 (2015).
5. Xu, S.-Y. et al. Discovery of a Weyl fermion semimetal and topological Fermi arcs. *Science* **349**, 613–617 (2015).
6. Nakatsuji, S., Kiyohara, N. & Higo, T. Large anomalous Hall effect in a non-collinear antiferromagnet at room temperature. *Nature* **527**, 212–215 (2015).
7. Kim, K. et al. Large anomalous Hall current induced by topological nodal lines in a ferromagnetic van der Waals semimetal. *Nat. Mater.* **17**, 794–799 (2018).
8. Sakai, A. et al. Giant anomalous Nernst effect and quantum-critical scaling in a ferromagnetic semimetal. *Nat. Phys.* **14**, 1119–1124 (2018).
9. Liu, D. F. et al. Magnetic Weyl semimetal phase in a Kagomé crystal. *Science* **365**, 1282–1285 (2019).
10. Liu, E. et al. Giant anomalous Hall effect in a ferromagnetic kagome-lattice semimetal. *Nat. Phys.* **14**, 1125–1131 (2018).
11. Belopolski, I. et al. Discovery of topological Weyl fermion lines and drumhead surface states in a room temperature magnet. *Science* **365**, 1278–1281 (2019).
12. Chang, G. et al. Magnetic and noncentrosymmetric Weyl fermion semimetals in the *R*AlGe family of compounds (*R* = rare earth). *Phys. Rev. B* **97**, 041104 (2018).
13. Suzuki, T. et al. Singular angular magnetoresistance in a magnetic nodal semimetal. *Science* **365**, 377–381 (2019).
14. Puphal, P. et al. Topological magnetic phase in the candidate Weyl semimetal CeAlGe. *Phys. Rev. Lett.* **124**, 017202 (2020).
15. Yang, H. Y. et al. Noncollinear ferromagnetic Weyl semimetal with anisotropic anomalous Hall effect. *Phys. Rev. B* **103**, 115143 (2021).
16. Wei, H. et al. Crystal structural refinement for NdAlSi. *Rare Metals* **25**, 355–358 (2006).
17. Lin, H., Rebelsky, L., Collins, M. F., Garret, J. D. & Buyers, W. J. L. Magnetic structure of UNi_2Si_2. *Phys. Rev. B* **43**, 13232 (1991).
18. Wu, S. et al. Incommensurate magnetism near quantum criticality in CeNiAsO. *Phys. Rev. Lett.* **122**, 197203 (2019).
19. Rossat-Mignod, J. et al. Phase diagram and magnetic structures of CeSb. *Phys. Rev. B* **16**, 440–461 (1977).
20. Gignoux, D. & Schmitt, D. Competition between commensurate and incommensurate phases in rare-earth systems: effects on *H-T* magnetic phase diagrams. *Phys. Rev. B* **48**, 12682 (1993).
21. Taylor, K. N. R. Intermetallic rare-earth compounds. *Adv. Phys.* **20**, 551–660 (1971).
22. Jensen, J. & Mackintosh, A. R. *Rare Earth Magnetism* (Clarendon Press, 1991).
23. Anisimov, V. I., Aryasetiawan, F. & Lichtenstein, A. I. First-principles calculations of the electronic structure and spectra of strongly correlated systems: the LDA+ *U* method. *J. Phys. Condens. Matter* **9**, 767 (1997).
24. Pizzi, G. et al. Wannier90 as a community code: new features and applications. *J. Phys. Condens. Matter* **31**, 165902 (2020).
25. Hosseini, M. V. & Askari, M. Ruderman-Kittel-Kasuya-Yosida interaction in Weyl semimetals. *Phys. Rev. B* **92**, 224435 (2015).
26. Chang, H.-R., Zhou, J., Wang, S.-X., Shan, W.-Y. & Di, X. RKKY interaction of magnetic impurities in Dirac and Weyl semimetals. *Phys. Rev. B* **92**, 241103(R) (2015).
27. Araki, Y. & Nomura, K. Spin textures and spin-wave excitations in doped Dirac-Weyl semimetals. *Phys. Rev. B* **93**, 094438 (2016).
28. Wang, S.-X., Hao-Ran Chang, H.-R. & Chang, H.-R. RKKY interaction in three-dimensional electron gases with linear spin-orbit coupling. *Phys. Rev. B* **96**, 115204 (2017).
29. Nikolić, P. Quantum field theory of topological spin dynamics. *Phys. Rev. B* **102**, 075131 (2020).
30. Nikolić, P. Dynamics of local magnetic moments induced by itinerant Weyl electrons. *Phys. Rev. B* **103**, 155151 (2021).

Methods

Crystal growth. We used a self-flux method to grow single crystals of NdAlSi. The starting materials were elemental Nd, Al and Si chunks with composition Nd/Al/Si = 1:10:1, mixed in an alumina crucible. The crucible was placed in a quartz tube, in which quartz wool was inserted as the strainer, and the tube was sealed under vacuum. The tube was placed in a box furnace, heated to 1,000 °C at 3 °C min^{-1}, held for 12 hours, cooled to 700 °C at 0.1 °C min^{-1}, maintained at 700 °C for 12 hours and then centrifuged to remove the Al flux.

Transport and magnetization measurements. Transport properties of NdAlSi were measured in a DynaCool physical property measurement system (Quantum Design). Electrical resistivity was measured with a standard four-probe technique, and the heat capacity was measured with a relaxation time method. The d.c. magnetization was measured using a vibrating sample magnetometer in a Quantum Design MPMS3. We measured quantum oscillations of resistivity in a 35 T d.c. Bitter magnet inside a ^{3}He fridge at a base temperature of 300 mK at the National High Magnetic Field Laboratory in Tallahassee. All samples used for transport measurements were carefully sanded to remove the residual Al flux and to have the ideal bar geometry for the determination of resistivity.

Second harmonic generation. The second harmonic generation data in the inset to Fig. 1c were taken at normal incidence on the [101] face of as-grown crystals for incoming/outgoing wavelengths of 1,500 nm/750 nm as a function of the incoming field polarization and measured for emitted light polarized parallel to the [010] crystalline axis. In this geometry, all bulk contributions to second harmonic generation from space group no. 141 are forbidden.

Neutron diffraction. The structure of NdAlSi was characterized by a single-crystal neutron time-of-flight diffraction experiment on TOPAZ at Oak Ridge National Laboratories. A 1 mm^3 sample of NdAlSi was mounted on a goniometer and cooled to 100 K. A three-dimensional neutron diffraction map was acquired for 13 different sample orientations, allowing coverage of 1,654 Bragg peaks. The nuclear structure factors were extracted from the three-dimensional datasets following a method reported by Schultz et al.[31]. The structural refinements were performed within space groups no. 109 and no. 141 using GSAS-II (ref. [32]).

The magnetic structure of NdAlSi was determined through various triple-axis neutron diffraction experiments using the BT-7, MACS and SPINS spectrometers, which are all located at the National Institute of Standards and Technology. These experiments were performed on single crystals of NdAlSi with a mass of ~50 mg aligned to collect diffraction data within the (*hk*0), (*hhl*) and (*h*0*l*) scattering planes for temperatures ranging from 1.5 K to 15 K. A 10 T vertical field magnet was used for the MACS experiment, which was performed with the **c** axis vertical such that the field dependence of the $(\frac{2}{3}, \frac{2}{3}, 0)$ Bragg peak intensity could be measured at 1.6 K for a field applied along the **c** axis. As on MACS, the order parameter measurements were acquired on SPINS with incident and scattered neutron energies of 3.7 meV. Cooled Be filters were employed before and after the sample. Rocking scans within the three magnetic phases of NdAlSi were collected using BT-7 to refine its magnetic structure as a function of temperature. We used pyrolytic graphite-filtered 35 meV neutrons for this work. The error bars for the diffraction data correspond to ±1 standard deviation.

DFT. The DFT calculations were performed in a plane-wave basis as implemented in the Vienna Ab initio Simulation Package[33,34] with the Perdew–Burke–Ernzerhof[35] generalized-gradient exchange–correlation functional. When the *f* electrons are included in the valence, the on-site correlation is taken into account using the DFT + *U* approximation with a range of Hubbard *U* values from 4 eV to 8 eV at the Nd *f* state. The results shown here are for the Hubbard *U* of 6 eV and a similar result was observed going to higher values of Hubbard *U*. Spin–orbit coupling was also included for all Nd ions as implemented in the pseudopotentials and appears to be an essential ingredient for topological properties in the presence of magnetism. We obtained a Wannier interpolation of the band structure near the Fermi level using Wannier90 (ref. [24]) and calculated the Weyl node positions using the WannierTools package[36]. A *k* point grid of 4 × 4 × 4 was used to discretize the first Brillouin zone. The relaxation of the atomic positions was carried out keeping the lattice parameters fixed at experimental values with the force criterion 10^{-2} eV Å^{-1}.

Data availability

All data needed to evaluate the conclusions in the paper are present in the paper and/or the Supplementary Information. Additional data related to this paper may be requested from the authors.

References

31. Schultz, A. J. et al. Integration of neutron time-of-flight single-crystal Bragg peaks in reciprocal space. *J. Appl. Crystallogr.* **47**, 915–921 (2014).
32. Toby, G. H. & Von Dreele, R. B. GSAS-II: the genesis of a modern open-source all purpose crystallography software package. *J. Appl. Crystallogr.* **46**, 544–549 (2013).
33. Kresse, G. & Furthmüller, J. Efficient iterative schemes for ab initio total-energy calculations using a plane-wave basis set. *Phys. Rev. B* **54**, 11169 (1996).
34. Kresse, G. & Joubert, D. From ultrasoft pseudopotentials to the projector augmented-wave method. *Phys. Rev. B* **59**, 11758 (1999).
35. Perdew, J. P., Burke, K. & Ernzerhof, M. Generalized gradient approximation made simple. *Phys. Rev. Lett.* **77**, 11758 (1996).
36. Wu, Q., Zhang, S., Song, H.-F., Troyer, M. & Soluyanov, A. A. WannierTools: an open-source software package for novel topological materials. *Comput. Phys. Commun.* **224**, 405–416 (2018).

Acknowledgements

This work was supported as part of the Institute for Quantum Matter, an Energy Frontier Research Center funded by the US Department of Energy, Office of Science, Basic Energy Sciences under award no. DE-SC0019331. The work at Boston College was funded by the National Science Foundation under award no. DMR-1708929. C.L.B. and J.G. were supported by the Gordon and Betty Moore Foundation through GBMF9456. A portion of this work was performed at the National High Magnetic Field Laboratory, which is supported by the National Science Foundation Cooperative Agreement no. DMR-1644779 and the state of Florida. We also acknowledge the support of the National Institute of Standards and Technology, US Department of Commerce. The identification of any commercial product or trade name does not imply endorsement or recommendation by the National Institute of Standards and Technology. Access to MACS was provided by the Center for High Resolution Neutron Scattering, a partnership between the National Institute of Standards and Technology and the National Science Foundation under agreement no. DMR-1508249. A portion of this research used resources at the Spallation Neutron Source, a Department of Energy Office of Science User Facility operated by the Oak Ridge National Laboratory. S.B. thanks J. Kim for fruitful discussions on the symmetric Wannier function generations from Wannier90. We thank Y. Li for useful discussions. We are also grateful to Y. Chen, Y. Luo, C. Lygouras and Y. Vekhov for their help during neutron scattering experiments.

Author contributions

The project was conceived by F.T., J.G., D.V. and C.L.B. Sample synthesis was done by H.-Y.Y. and F.T., and D.H.T. and B.L. performed and analysed the second harmonic generation experiments. The heat capacity and bulk susceptibility measurements were carried out by H.-Y.Y. and analysed by J.G. Neutron scattering experiments were performed by J.G., C.L.B., G.X., Y.Z., J.A.R.-R. and C.M.H. The neutron analysis was performed by J.G. Quantum oscillation measurements were conducted and analysed by H.-Y.Y., F.T. and D.E.G. The DFT calculations were carried out by S.B. and D.V.; P.N. interpreted the data in terms of his theory of exchange interactions mediated by Weyl electrons. The first draught of the paper was written by J.G., H.-Y.Y. and S.B., and all authors contributed with comments and edits.

Competing interests

The authors declare no competing interests.

Additional information

Supplementary information The online version contains supplementary material available at https://doi.org/10.1038/s41563-021-01062-8.

Correspondence and requests for materials should be addressed to J.G.

Peer review information *Nature Materials* thanks Philippe Bourges and the other, anonymous, reviewer(s) for their contribution to the peer review of this work.

Reprints and permissions information is available at www.nature.com/reprints.